# LANDFAST ICEBERG HEIGHT RETRIEVAL AND EVALUATION BASED ON REMOTE SENSING APPROACHES IN ANTARCTICA

L. Wang[1, 2], G. Qiao[1, 2]*, I.V. Florinsky[3], S. Popov[4,5]

[1] Centre for Spatial Information Science and Sustainable Development, Tongji University, 1239 Siping Road, Shanghai, China - (lijuan_wang, qiaogang)@tongji.edu.cn
[2] College of Surveying and Geo-Informatics, Tongji University, 1239 Siping Road, Shanghai, China
[3] Institute of Mathematical Problems of Biology Keldysh, Institute of Applied Mathematics, Russian Academy of Sciences, Pushchino, Russia - iflor@mail.ru
[4] Saint Petersburg State University, 7-9 Universitetskaya Emb., St. Petersburg 199034, Russia - spopov67@yandex.ru
[5] Polar Marine Geosurvey Expedition (PMGE), 24, Pobedy str., Lomonosov, St. Petersburg, 198412, Russia

**Commission TCIII, WG III/9**

**KEY WORDS:** Remote sensing, Satellite, Unmanned aerial vehicle (UAV), Iceberg, Height retrieval.

**ABSTRACT:**

Icebergs are one of the important components of Antarctic ice loss, and their spatial distribution and volume changes have a profound impact on ocean circulation, sea ice formation, freshwater balance and carbon cycle in the Southern Ocean, and ship navigation. Therefore, effective monitoring of icebergs is of great significance. Iceberg height is an important parameter of iceberg volume, and its accurate estimation is crucial to the calculation of iceberg thickness and volume. In this paper, based on optical satellite images, satellite altimetry data and digital surface model (DSM) derived from unmanned aerial vehicle (UAV), the iceberg height retrieval approaches were studied, including shadow based, satellite altimetry based and DSM based methods. Then, the results of different approaches were evaluated and analyzed by taking icebergs in the landfast ice area as an example. Finally, we concluded that all three methods could effectively extract the height information of icebergs. For the shadow-height method with relatively low accuracy, lower sun altitude and higher icebergs would be more conducive to accurate height estimation.

## 1. INTRODUCTION

Icebergs are free-floating ice blocks formed by the fragmentation of ice shelves, glacier edges, or larger icebergs (Cuffey & Paterson, 1994; Wesche et al., 2012), which account for half of the total Antarctic ice loss (Depoorter et al., 2013; Rignot et al., 2013). The calving of icebergs instantly weakens the buttressing effect of ice shelves or glaciers (Dupont et al., 2005; Fürst et al., 2016), which intensifies ice shelf or glacier flow by changing the dynamics of ice and causing ice sheet flow to accelerate. The retreat and collapse of glaciers constitute a significant part of the ice discharge from ice sheets to the ocean, leading to sea level rise (Ingels et al., 2021).

The drift and melting of icebergs have profound effects on the marine environment and ship navigation (Han et al., 2019). Floating icebergs drift under the influence of the ocean, atmosphere, sea ice, and other complex environments (Koo et al., 2021), which provide a good indication of ocean circulation (Collares et al., 2018), but also pose a threat to marine operations (Ressel et al., 2015). Meltwater from icebergs, especially from super-large ones, has important implications for the freshwater balance of the entire Southern Ocean (Silva et al., 2006). The melting of icebergs releases relatively cold fresh water into the ocean, changes the thermosaline structure of the sea surface, and promotes convection between the overlying water layer and the bottom deep water while lowering the ocean surface temperature (Jenkins, 1999). At the same time, the cold fresh water produced by the melting of icebergs is also a key component of sea ice formation (Merino et al., 2016), and the water mass transformation that occurs during this freezing and thawing process affects local ocean circulation and even affects the entire climate system on a larger spatial scale (Robinson & Williams, 2012; Barbat et al., 2021). In addition, the abundant iron content in iceberg meltwater provides nutrients for phytoplankton growth and marine production in the Southern Ocean, and plays an important role in carbon cycling and marine carbon uptake in the Southern Ocean (Laufkötter et al. , 2018). Therefore, effective monitoring and tracking of icebergs are essential to study the global freshwater cycle and risk aversion in polar scientific expeditions.

The earliest ship-based iceberg observations were limited by the harsh environment in polar regions and could only collect information on the size and distribution of icebergs in limited time and space (Jacka & Giles, 2007). With the rapid development of spaceborne sensors, remote sensing data is increasingly used in polar research, enabling iceberg detection with wide coverage and high temporal resolution. Icebergs can be easily observed from image data collected from optical sensors. High-resolution optical images can provide detailed information on iceberg distribution (Rezvanbehbahani et al., 2019), but they are easily limited by cloud cover or light intensity and cannot obtain effective ground information. Due to its advantage of being independent of weather and light conditions, microwave remote sensing enables iceberg monitoring in almost all meteorological conditions (Dammann et al., 2019). The U.S. National Ice Center (NIC) and Brigham Young University (BYU) have systematically tracked giant icebergs using scatterometer data with lower spatial resolution (Stuart & Long, 2011), and Budge & Long (2018) have updated the iceberg tracking database on this basis. Synthetic Aperture Radar (SAR) technology has been widely used in the study of

* Corresponding author

iceberg monitoring. According to the radar backscattering difference between the iceberg and the surrounding environment, higher-resolution iceberg information can be obtained (Wesche et al., 2012). Many studies have developed automatic iceberg detection methods based on SAR or Advanced Synthetic Aperture Radar (ASAR) images, extracting the distribution of icebergs off the coast of Antarctica (Wesche & Dierking, 2015; Mazur et al., 2017), and tracking the changes in the location, area, and direction of iceberg targets through long-term observations (Barbat et al., 2021; Koo et al., 2021).

Iceberg height (or freeboard), as an important parameter in iceberg detection and tracking, is essential in the study of iceberg volume, which is important for factors such as iceberg classification (Dammann et al., 2019), iceberg stability (Guttenberg et al., 2011), and optimization of parameters in climate models (Braakmann-Folgmann et al., 2021). Measurements of iceberg freeboard using satellite altimeter data have been used to study iceberg thickness since the late 1980s (McIntyre & Cudlip, 1987). Several studies of giant tabular icebergs extracted freeboard from elevation data measured by radar and laser altimeters, such as CryoSat-2 (Han et al., 2019; Braakmann-Folgmann et al., 2021; Koo et al., 2021) and ICESat-2 (Koo et al., 2021) altimetry data, which were used to determine the variation of the iceberg freeboard and then estimate the iceberg thickness from the iceberg freeboard under the assumption of hydrostatic equilibrium, combined with the iceberg area obtained from satellite images to monitor iceberg volume change. In addition, the DSM constructed by optical satellite stereophotogrammetry was also used to extract iceberg freeboard and calculate the volume (Enderlin & Hamilton, 2014). For a single optical image, the elevation information of the object cannot be obtained, but the shadow-height method can make full use of the length information of the shadow cast by the object in the optical remote sensing image to estimate its height. This method is commonly used to obtain the height of buildings (Irvin & McKeown, 1989; Shao et al., 2011; Liasis & Stavrou, 2016), and in a recent study, the method was applied to the inversion of iceberg freeboard and achieved good results (Guan et al., 2021).

The above-mentioned measurement methods of iceberg height have been verified in the study of polar icebergs, but the comparison of different methods is still lacking. Therefore, in this paper, based on multi-source remote sensing data of satellite and unmanned aerial vehicle (UAV), three different approaches for iceberg height retrieval are developed, and the applicability of these methods is evaluated and analyzed by using landfast icebergs.

## 2. DATA AND METHODS

### 2.1 Study Area

The study area of this paper is located in the waters of Prydz Bay near Zhongshan Station, China (Figure 1), which is widely distributed with landfast sea ice during winter time, dominated by first-year sea ice (FYI), which can extend from the coast to about 30 km range, with thicknesses ranging from 1.5 m to 2.0 m (Lei et al., 2010; Hui et al., 2017). Many icebergs calving from ice shelves or glaciers float into the bay under the constant influence of currents and winds, where they become stranded when surrounded by landfast sea ice. The large and evenly distributed landfast sea ice provides a good height reference plane for the inversion of iceberg heights and is an ideal area for experimenting with different methods. It should be noted that the iceberg height in this study represents the height relative to the fixed ice surface, not the water outlet height or full freeboard of the iceberg.

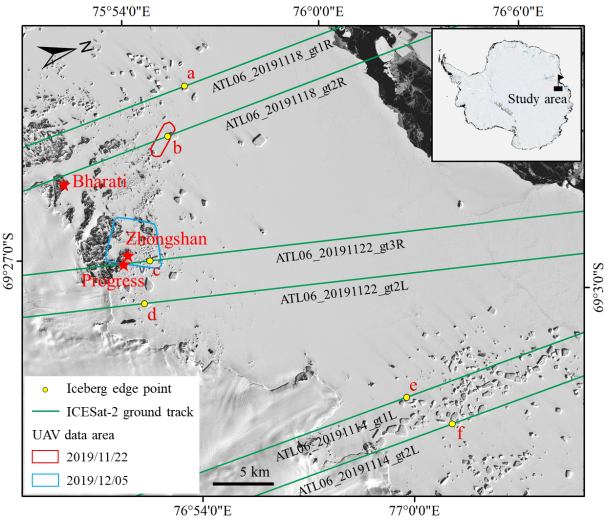


**Figure 1**. Location of the study area (inset) and experiment data (UAV data and ICESat-2 ground track) overlaid on Sentinel-2 optical image captured on September 30, 2019.

### 2.2 Remote Sensing Data

**2.2.1 Sentinel-2 Image Data**: In this paper, the Sentinel-2 satellite optical image data was used to invert the height of the iceberg, and the height of the iceberg was calculated by measuring the shadow length of the iceberg in the optical image. The Sentinel-2 mission consists of a constellation of two polar-orbiting satellites (2A and 2B) in the same sun-synchronous orbit, 180° relative to each other. The Sentinel-2A satellite was launched in June 2015, and the Sentinel-2B satellite was launched in March 2017. Each satellite of Sentinel-2 carries a Multi-Spectral Instrument (MSI), which can cover 13 spectral bands with a width of 290 km and a spatial resolution of 10 m, 20 m, and 60 m. The revisit period of a satellite is 10 days, and two satellites can provide a high revisit frequency of 5 days. This study used the Level-2A data from Sentinel-2B (Table 1), which was downloaded from the European Space Agency (ESA) website (https://sentinel.esa.int/web/sentinel/home). The Level-2A data is the atmospheric bottom reflectance data after atmospheric correction. The blue band (Band 2) with a resolution of 10 meters was selected for data processing.

| Platform | Acquisition data and time | Resolution (m) |
|---|---|---|
| Sentinel-2B | 2019/09/30 03:46:29.024Z | 10 |
| | 2019/10/30 03:46:29.024Z | 10 |
| | 2019/12/19 03:46:19.024Z | 10 |

| Platform | Acquisition data | Area (km$^2$) | GSD (cm) |
|---|---|---|---|
| DJI Phantom 4 RTK | 2019/11/22 | 2.824 | 8.89 |
| | 2019/12/05 | 14.962 | 7.82 |

**Table 1**. Sentinel-2 images and UAV data used in this study.

**2.2.2 ICESat-2 Altimetry Data**: Satellite altimetry data provides ground elevation information and is used in this paper to invert iceberg heights. The Ice, Cloud, and Land Elevation Satellite-2 (ICESat-2), a second laser altimetry satellite after ICESat, was launched by the National Aeronautics and Space Administration (NASA) on September 15, 2018. The satellite carries the Advanced Topographic Laser Altimeter System (ATLAS), which uses a low-energy green (532 nm) laser with single-photon sensitive detectors to measure distances and is used to measure changes in elevation of ice sheets and glaciers, as well as sea ice freeboard distribution (Markus et al., 2017; Neumann et al., 2019). ICESat-2 obtains surface elevation information of the Earth using three pairs of beams, separated by about 3 km, each paired at 90 m spacing and with a sampling interval of 0.7 m along the track. We used the ATL06 version 3 data product of ICESat-2 to conduct experiments, downloaded from the National Snow & Ice Data Center (NSIDC) website (https://nsidc.org/data/ATL06/versions/3). The ATL06 data is a Level-3A product and contains the mean land ice surface height averaged along 40 m segments of ground track and spaced 20 m apart, which is the height above the World Geodetic System 1984 (WGS84) ellipsoid (Smith et al., 2019; Smith et al., 2020).

**2.2.3 UAV Data**: The application of UAV in the field of remote sensing provides the possibility for high-precision three-dimensional (3D) modelling of the surface, especially for the study of ice and snow environments in polar regions with challenging conditions (Li et al., 2019). In this study, we generated the ortho-mosaic and DSM of the landfast sea ice surface based on UAV data collected by DJI Phantom 4 RTK and D-RTK 2 in the 36th Chinese National Antarctic Research Expedition (CHINARE). The details of the UAV surveys used are listed in Table 1. The modelling of UAV data is based on the automatic image matching algorithm of optical stereo images to realize the 3D reconstruction of the terrain surface. Yuan et al. (2020) demonstrated that the DJI Phantom 4 RTK photogrammetry without ground control points (GCPs) can achieve centimeter-level relative mapping accuracy through UAV flight experiments with different geo-positioning approaches, and that there is a meter-level offset caused by the D-RTK 2 positioning error. In order to verify the applicability of DJI UAV technology in polar regions, He et al. (2021) evaluated the UAV 3D model based on ICESat-2 elevation points and concluded that the UAV modeling results can achieve acceptable results without GCPs. In this study, we used the Pix4D Mapper software developed by the Swiss Pix4D company to process the collected data by structure-from-motion multi-view stereo technology (SfM-MVS) without GCPs and generate ortho-mosaic and DSM products based on the WGS84 ellipsoid. Data processing includes three main steps. First, the software automatically extracts feature points from image data, finds connection points from adjacent image pairs, and optimizes camera parameters through bundle adjustment. Then, dense point clouds and 3D textured meshes are generated according to the optimized camera parameters. Finally, DSM and ortho-mosaic are exported according to the user-defined spatial resolution.

### 2.3 Iceberg Height Retrieval

**2.3.1 Shadow Based Iceberg Height Retrieval**: The shadows of objects in optical remote sensing images provide effective information for the estimation of object height. According to the geometric relationship between iceberg height (H), shadow length (L) along sun azimuth (As) and sun altitude (Hs) (Figure 3), the iceberg height (H) can be estimated by:

$$H = L \tan Hs \tag{1}$$

The sun altitude and azimuth are calculated according to geographic latitude $\varphi$, sun declination $\delta$, and hour angle $\omega$ (He et al., 2008; Yu et al., 2017):

$$\sin Hs = \sin\varphi \sin\delta + \cos\varphi \cos\delta \cos\omega \tag{2}$$

$$\sin As = -\frac{\cos\delta \sin\omega}{\cos Hs} \tag{3}$$

$$\delta = 23.45 \sin\left(\frac{2\pi(284+n)}{365}\right) \tag{4}$$

$$\omega = 15(t_s - 12) \tag{5}$$

where $n$ = date serial number accumulated since January 1
$t_s$ = solar time

Considering the difference in the shadow length of icebergs at different sun altitude angles and their possible influence on the accuracy of the results, we selected three Sentinel-2 optical remote sensing image data at different times to carry out the above experiments. The relevant information of the data is shown in Table 1. The process of calculating the iceberg height is shown in Figure 2, and the specific steps are as follows:

Step 1. According to visual interpretation, select the iceberg edge point (point A in Figure 3) in the image, and extract the latitude and longitude information of the point;

Step 2. Obtain the acquisition date and time of the image data, and combine it with the latitude and longitude information of the iceberg edge point to calculate the solar altitude Hs and solar azimuth As at the location;

Step 3. Using the sun azimuth As obtained in the previous step, determine the direction of the iceberg shadow with reference to true north, and then measure the length L (the length of the AB line segment in Figure 3) of the iceberg shadow along this direction;

Step 4. Based on simple trigonometry, calculate the iceberg height H (H in the inset of Figure 3).

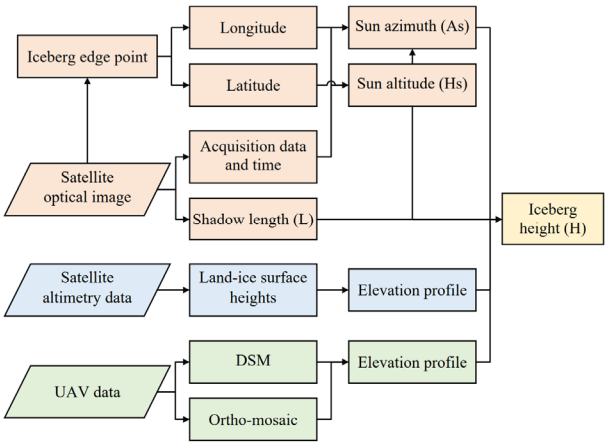


**Figure 2**. Flowchart of iceberg height retrieval by three different methods.

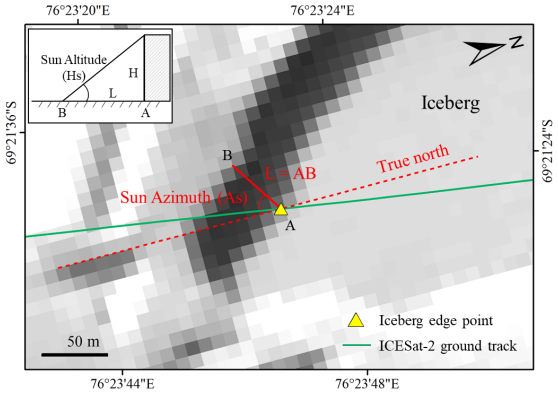


**Figure 3**. The geometric relationship between iceberg height (H), shadow length (L) along sun azimuth (As), and sun altitude (Hs). Take the iceberg "c" in Figure 1 as an example.

**2.3.2 Satellite Altimetry Based Iceberg Height Retrieval**: Land ice surface heights measured by satellite laser can provide a direct measurement of iceberg height. By plotting the along-track elevation profile and extracting continuous elevation data at the edge of the iceberg, the height H of the iceberg can be obtained based on the height difference (Figure 2). In order to compare the capabilities of different methods, we filtered the ICESat-2 ATL06 data whose ground track passed through the iceberg in order to carry out the above experiments under the premise of ensuring the complete shadow of the iceberg. Figure 1 shows the spatial distribution of the data used. Taking iceberg "c" in Figure 1 as an example, the height of the iceberg was directly obtained by subtracting the elevation of the sea ice surface from the elevation of the iceberg edge in the altimetry data profile (Figure 4c). Note that the land ice height data provided by ATL06 is invalid at the edge of icebergs with large surface slopes due to the limitation of model residuals when the ATL06 algorithm fits the ATL03 photon data to 40 m segments (Smith et al., 2019). Therefore, in the elevation profile of satellite altimetry data, there is a certain deviation between the elevation abrupt point near the edge of the iceberg and the actual iceberg edge point, and this deviation should be considered in the analysis of the results.

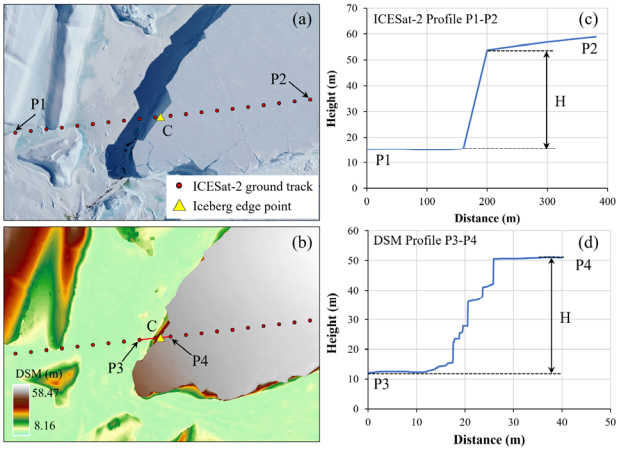


**Figure 4**. (a) Ortho-mosaic and ICESat-2 ground track points. (b) DSM and ICESat-2 ground track points. (c) The elevation profile of ICESat-2. (d) The elevation profile of DSM.

**2.3.3 DSM Based Iceberg Height Retrieval**: Similar to the satellite altimetry based method, the iceberg height H based on the UAV data product DSM is also extracted from the continuous elevation profile at the edge of the iceberg (Figure 2). We used the data collected from the two UAV surveys listed in Table 1 to construct a 3D model of the sea ice surface. Within the coverage of these two missions, an iceberg was selected for height estimation, and the selected iceberg was also included in the experiments of the other two retrieval methods, so that the three methods could be compared and analyzed. The elevation profile was plotted along the ICESat-2 ground track, and the endpoints were the two vertices where the elevation value of the ATL06 elevation profile changed abruptly. Then, the iceberg height H was obtained by taking the difference between the elevations of the two points (Figure 4d).

## 3. RESULTS AND DISCUSSION

### 3.1 Iceberg Height Evaluation

Using the above-mentioned landfast iceberg height retrieval approaches, we conducted experiments based on satellite optical and altimetry data and UAV data products, respectively, and evaluated the accuracy of these methods by comparing the results of different iceberg heights (Table 2). Shen et al. (2021) estimated that the accuracy of the ICESat-2 ATL06 elevation product was less than 0.14 m by comparing the near-coincident measurements from the Airborne Topographic Mapper (ATM) and ICESat-2 ATLAS at the marginal and interior Antarctic Ice Sheet, demonstrating the centimeter-scale accuracy of the ICESat-2 land ice surface heights and the reliability of the ground elevation data provided. Therefore, in this study, we chose the iceberg height retrieved from satellite altimetry data as the true value reference to verify the accuracy of the results of the other two methods. We first evaluated the accuracy of shadow-height and DSM-height methods based on the iceberg height calculated by the satellite altimetry-height method, and then analyzed the effects of sun altitude and iceberg height on the accuracy of the results for shadow-based iceberg height retrieval.

The results and accuracy evaluation of the three landfast iceberg height retrieval approaches are shown in Table 1. Three methods were applied to the height retrieval of two icebergs, "c" and "d" (Figure 1), as described in Section 2.3.3. It can be found that the DSM-height method can achieve sub-meter accuracy. Although the shadow-height method cannot achieve the same high accuracy as the former, it still shows satisfactory results. For iceberg "d", the height error of ~1 m is mainly due to the shadow length error of ~1.3 m, which is considered acceptable for the image data of 10 m pixel size under the assumption of ignoring the sun altitude error.

| Method | Shadow-height | Satellite altimetry-height | DSM-height | Iceberg |
|---|---|---|---|---|
| **Data product** | Sentinel-2 | ICESat-2 | UAV | |
| **Acquisition data** | 2019/12/19 | 2019/11/18 | 2019/11/22 | |
| **Iceberg height (m)** | 50.253 | 49.274 | 49.347 | d |
| **Error (m)** | 0.979 | -- | 0.073 | |
| **Relative Error (%)** | 1.99 | -- | 0.15 | |
| **Data product** | Sentinel-2 | ICESat-2 | UAV | |
| **Acquisition data** | 2019/12/19 | 2019/11/22 | 2019/12/05 | |
| **Iceberg height (m)** | 36.452 | 38.330 | 38.869 | c |
| **Error (m)** | -1.878 | -- | 0.539 | |
| **Relative Error (%)** | -4.90 | -- | 1.41 | |

**Table 2**. Details of experiment data and results comparisons. The icebergs "d" and "c" correspond to the icebergs in Figure 1.

Lower solar altitude is thought to enable precise measurements of iceberg freeboard (Guan et al., 2021), since iceberg shadow on landfast ice surface is longer at low solar altitude. In addition, for the image data acquired at the same time, icebergs with different heights will also form shadows of different lengths. Therefore, the height of icebergs also has a certain degree of influence on the accuracy of the retrieval results. In order to explore the influence of these two factors on the shadow-height method, we used Sentinel-2 optical remote sensing images collected at three different times (Table 1; September 30, 2019, October 30, 2019, and December 19, 2019) to estimate iceberg heights, and the errors of all iceberg heights are plotted in Figure 5. The three line graphs correspond to the times of the three image data, respectively, representing different solar heights. The solar height on September 30, 2019 is the smallest, and the solar height on December 19, 2019 is the largest.

As experience suggests, lower solar altitude corresponds to a more precise iceberg height. At the same time, it can also be seen from Figure 5 that icebergs with higher heights show better retrieval results. For the September 30, 2019 experiment, the error for the iceberg "f" is slightly larger but within meters. In order to analyze the cause of this phenomenon, we supplemented the Sentinel-2 image data on December 29, 2019 on the basis of the satellite images mentioned above three times and further observed the landfast ice environment in the study area (Figure 6). As can be seen from the time-series images, as the Antarctic summer arrives, the rise in temperature causes the landfast ice to continue to break off at the edge near iceberg "f". But on the bottoms of sea ice and icebergs that cannot be seen through images, these places may have melted before, or even earlier. The melting of ice changes the thickness of landfast ice and icebergs, which may bring about changes in elevation due to the buoyancy of seawater, and the tidal action of seawater may also cause changes in elevation. The true reference height of iceberg "f" was obtained from the ICESat-2 ATL06 altimetry data on November 14, 2019, and there was a long time interval between this time and the acquisition date of the optical image (September 30, 2019). Bottom melting of the iceberg may have occurred during this time, creating a slightly larger gap between the two height results.

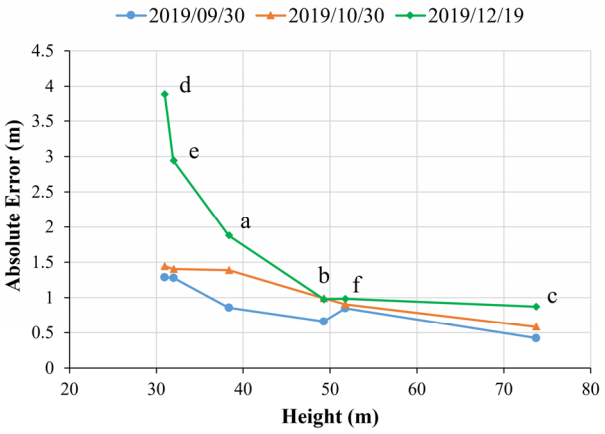


**Figure 5**. The relationship between the sun altitude/iceberg height and the accuracy of results. The labels a-e correspond to the icebergs in Figure 1.

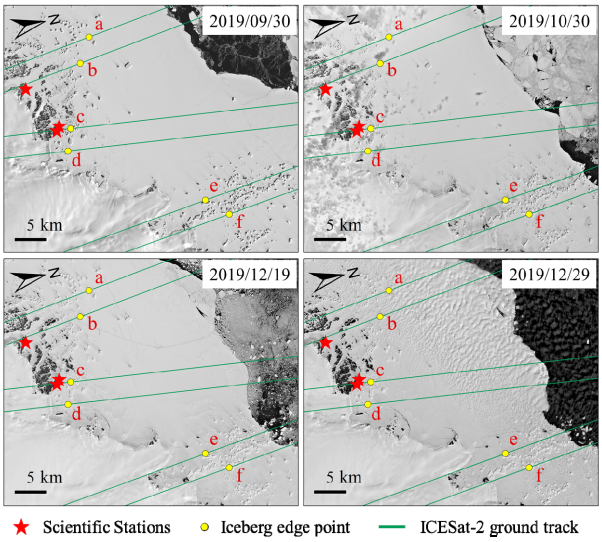


**Figure 6**. The time series of Sentinel-2 satellite optical images. The iceberg edge points and ICESat-2 ground tracks used for the retrieval experiment are marked above, and the information of the three scientific stations is shown in Figure 1.

### 3.2 Applicability and Uncertainty Analysis

The experimental results presented in this paper show that the iceberg height retrieval based on satellite optical images, satellite altimetry data, and UAV data products can achieve satisfactory results, but the applicability and uncertainty of different methods are different. Each method is discussed separately below. The wide coverage of satellite optical images makes it possible to extract iceberg heights on a large scale. But for 10m resolution image data, the iceberg shadow length of one pixel may lead to a large height error, which can be several meters or even tens of meters in this experiment. In addition, cloud occlusion of image data and incomplete projection of icebergs also limit the use of shadow based method. The satellite altimetry data can reach centimeter-level accuracy, but it can only measure the height of the iceberg covered by the ground track, and due to the absence of the elevation value at the edge of the iceberg, the calculated edge height of the iceberg is offset from the actual value. This situation has less effect on the edges of tabular icebergs. The ground model constructed by the UAV using the data collected by the airborne platform also has high precision, providing fine observation data for the detection of surface feature information. However, due to the complex environmental factors in the polar regions, the execution of UAV flight missions faces many challenges, so the coverage of data is limited and the quantity is small.

## 4. CONCLUSIONS

In this study, based on Sentinel-2 satellite imagery, ICESat-2 ATL06 altimetry data, and DJI Phantom 4 RTK UAV data product DSM, we used three iceberg height retrieval methods to extract iceberg heights in the landfast ice area near Zhongshan Station, respectively. When analyzing the accuracy of the method, we selected the iceberg height estimated by the satellite altimetry based method as the true value reference, and evaluated the results of the shadow based and DSM based methods. The effects of sun altitude and iceberg height on the results precision of the shadow-based method were also considered. The results show that the error of the iceberg height estimated by the DSM-height method can be controlled within the meter level, and the error of the shadow-height method is

larger, but it is acceptable compared to the 10 m resolution image data. In addition, low solar altitude and high iceberg height are more favorable for iceberg height retrieval. Finally, the applicability and uncertainty factors of the three methods were analyzed and discussed. In future work, how to integrate multi-source remote sensing data to realize the extraction of large-scale iceberg height and monitoring of its changes, and then to estimate the melting of the bottom of the iceberg, needs further research.

## ACKNOWLEDGEMENTS

This research was supported by the Natural Science Foundation of China (No. 42011530088, 41941006, 41771471), and the Fundamental Research Funds for the Central Universities.

## REFERENCES

Barbat, M. M., Rackow, T., Wesche, C., Hellmer, H. H., & Mata, M. M., 2021. Automated iceberg tracking with a machine learning approach applied to SAR imagery: A Weddell sea case study. *ISPRS Journal of Photogrammetry and Remote Sensing*, 172, 189-206.

Braakmann-Folgmann, A., Shepherd, A., & Ridout, A., 2021. Tracking changes in the area, thickness, and volume of the Thwaites tabular iceberg "B30" using satellite altimetry and imagery. *The Cryosphere*, 15(8), 3861-3876.

Budge, J. S., & Long, D. G., 2018. A comprehensive database for Antarctic iceberg tracking using scatterometer data. *IEEE Journal of Selected Topics in Applied Earth Observations and Remote Sensing*, 11(2), 434-442.

Collares, L. L., Mata, M. M., Kerr, R., Arigony-Neto, J., & Barbat, M. M., 2018. Iceberg drift and ocean circulation in the northwestern Weddell Sea, Antarctica. *Deep Sea Research Part II: Topical Studies in Oceanography*, 149, 10-24.

Cuffey, K. M., & Paterson, W. S. B., 2010: *The physics of glaciers*. Academic Press.

Dammann, D. O., Eriksson, L. E., Nghiem, S. V., Pettit, E. C., Kurtz, N. T., Sonntag, J. G., ... & Mahoney, A. R., 2019. Iceberg topography and volume classification using TanDEM-X interferometry. *The Cryosphere*, 13(7), 1861-1875.

Dammann, D. O., Eriksson, L. E., Nghiem, S. V., Pettit, E. C., Kurtz, N. T., Sonntag, J. G., ... & Mahoney, A. R., 2019. Iceberg topography and volume classification using TanDEM-X interferometry. *The Cryosphere*, 13(7), 1861-1875.

Depoorter, M. A., Bamber, J. L., Griggs, J. A., Lenaerts, J. T., Ligtenberg, S. R., van den Broeke, M. R., & Moholdt, G., 2013. Calving fluxes and basal melt rates of Antarctic ice shelves. *Nature*, 502(7469), 89-92.

Dupont, T. K., & Alley, R. B., 2005. Assessment of the importance of ice-shelf buttressing to ice-sheet flow. *Geophysical Research Letters*, 32(4).

Enderlin, E. M., & Hamilton, G. S., 2014. Estimates of iceberg submarine melting from high-resolution digital elevation models: application to Sermilik Fjord, East Greenland. *Journal of Glaciology*, 60(224), 1084-1092.

Fürst, J. J., Durand, G., Gillet-Chaulet, F., Tavard, L., Rankl, M., Braun, M., & Gagliardini, O., 2016. The safety band of Antarctic ice shelves. *Nature Climate Change*, 6(5), 479-482.

Guan, Z., Cheng, X., Liu, Y., Li, T., Zhang, B., & Yu, Z., 2021. Effectively Extracting Iceberg Freeboard Using Bi-Temporal Landsat-8 Panchromatic Image Shadows. *Remote Sensing*, 13(3), 430.

Guttenberg, N., Abbot, D. S., Amundson, J. M., Burton, J. C., Mac Cathles, L., MacAYEAL, D. R., & Zhang, W. W., 2011. A computational investigation of iceberg capsize as a driver of explosive ice-shelf disintegration. *Annals of Glaciology*, 52(59), 51-59.

Han, H., Lee, S., Kim, J. I., Kim, S. H., & Kim, H. C., 2019. Changes in a Giant Iceberg Created from the Collapse of the Larsen C Ice Shelf, Antarctic Peninsula, Derived from Sentinel-1 and CryoSat-2 Data. *Remote Sensing*, 11(4), 404.

He, X., Yu, H., Li, J., Ding, L., 2008. An engineering formula solution for the solar azimuth and its application. *Acta Energiae Solaris Sinica*, 29(1), 69.

He, Y., Qiao, G., Li, H., Yuan, X., & Li, Y., 2021. Unmanned Aerial Vehicle Derived 3d Model Evaluation Based on ICESAT-2 for Ice Surface Micro-Topography Analysis in East Antarctica. *The International Archives of Photogrammetry, Remote Sensing and Spatial Information Sciences*, 43, 463-468.

Hui, F., Zhao, T., Li, X., Shokr, M., Heil, P., Zhao, J., ... & Cheng, X., 2017. Satellite-based sea ice navigation for Prydz Bay, East Antarctica. *Remote Sensing*, 9(6), 518.

Ingels, J., Aronson, R. B., Smith, C. R., Baco, A., Bik, H. M., Blake, J. A., ... & Zamora-Duran, M. A., 2021. Antarctic ecosystem responses following ice-shelf collapse and iceberg calving: Science review and future research. *Wiley Interdisciplinary Reviews: Climate Change*, 12(1), e682.

Irvin, R. B., & McKeown, D. M., 1989. Methods for exploiting the relationship between buildings and their shadows in aerial imagery. *IEEE Transactions on Systems, Man, and Cybernetics*, 19(6), 1564-1575.

Jacka, T. H., & Giles, A. B., 2007. Antarctic iceberg distribution and dissolution from ship-based observations. *Journal of Glaciology*, 53(182), 341-356.

Jenkins, A., 1999. The impact of melting ice on ocean waters. *Journal of physical oceanography*, 29(9), 2370-2381.

Koo, Y., Xie, H., Ackley, S. F., Mestas-Nuñez, A. M., Macdonald, G. J., & Hyun, C. U., 2021. Semi-automated tracking of iceberg B43 using Sentinel-1 SAR images via Google Earth Engine. *The Cryosphere*, 15(10), 4727-4744.

Laufkötter, C., Stern, A. A., John, J. G., Stock, C. A., & Dunne, J. P., 2018. Glacial iron sources stimulate the southern ocean carbon cycle. *Geophysical Research Letters*, 45(24), 13-377.

Lei, R., Li, Z., Cheng, B., Zhang, Z., & Heil, P., 2010. Annual cycle of landfast sea ice in Prydz Bay, east Antarctica. *Journal of Geophysical Research: Oceans*, 115(C2).

Li, T., Zhang, B., Cheng, X., Westoby, M. J., Li, Z., Ma, C., ... & Li, X., 2019. Resolving Fine-Scale Surface Features on Polar

Sea Ice: A First Assessment of UAS Photogrammetry Without Ground Control. *Remote Sensing*, 11(7), 784.

Liasis, G., & Stavrou, S., 2016. Satellite images analysis for shadow detection and building height estimation. *ISPRS Journal of Photogrammetry and Remote Sensing*, 119, 437-450.

Markus, T., Neumann, T., Martino, A., Abdalati, W., Brunt, K., Csatho, B., ... & Zwally, J., 2017. The Ice, Cloud, and land Elevation Satellite-2 (ICESat-2): science requirements, concept, and implementation. *Remote sensing of environment*, 190, 260-273.

Mazur, A. K., Wåhlin, A. K., & Krężel, A., 2017. An object-based SAR image iceberg detection algorithm applied to the Amundsen Sea. *Remote Sensing of Environment*, 189, 67-83.

McIntyre, N. F., & Cudlip, W., 1987. Observation of a giant Antarctic tabular iceberg by satellite radar altimetry. *Polar Record*, 23(145), 458-462.

Merino, N., Le Sommer, J., Durand, G., Jourdain, N. C., Madec, G., Mathiot, P., & Tournadre, J., 2016. Antarctic icebergs melt over the Southern Ocean: Climatology and impact on sea ice. *Ocean Modelling*, 104, 99-110.

Neumann, T. A., Martino, A. J., Markus, T., Bae, S., Bock, M. R., Brenner, A. C., ... & Thomas, T. C., 2019. The Ice, Cloud, and Land Elevation Satellite–2 Mission: A global geolocated photon product derived from the advanced topographic laser altimeter system. *Remote Sensing of Environment*, 233, 111325.

Ressel, R., Frost, A., & Lehner, S., 2015. Navigation assistance for ice-infested waters through automatic iceberg detection and ice classification based on TerraSAR-X imagery. *The International Archives of Photogrammetry, Remote Sensing and Spatial Information Sciences*, 40(7), 1049.

Rezvanbehbahani, S., Stearns, L. A., Keramati, R., & Shankar, S., 2019. Automating iceberg detection in Greenland using deep learning on high to moderate-resolution optical imagery. *In AGU Fall Meeting Abstracts*, C31A-1490.

Rignot, E., Jacobs, S., Mouginot, J., & Scheuchl, B., 2013. Ice-shelf melting around Antarctica. *Science*, 341(6143), 266-270.

Robinson, N. J., & Williams, M. J. M., 2012. Iceberg-induced changes to polynya operation and regional oceanography in the southern Ross Sea, Antarctica, from in situ observations. *Antarctic Science*, 24(5), 514-526.

Shao, Y., Taff, G. N., & Walsh, S. J., 2011. Shadow detection and building-height estimation using IKONOS data. *International journal of remote sensing*, 32(22), 6929-6944.

Shen, X., Ke, C. Q., Yu, X., Cai, Y., & Fan, Y., 2021. Evaluation of Ice, Cloud, And Land Elevation Satellite-2 (ICESat-2) land ice surface heights using Airborne Topographic Mapper (ATM) data in Antarctica. *International Journal of Remote Sensing*, 42(7), 2556-2573.

Silva, T. A. M., Bigg, G. R., & Nicholls, K. W., 2006. Contribution of giant icebergs to the Southern Ocean freshwater flux. *Journal of Geophysical Research: Oceans*, 111(C3).

Smith, B., Fricker, H. A., Holschuh, N., Gardner, A. S., Adusumilli, S., Brunt, K. M., ... & Siegfried, M. R., 2019. Land ice height-retrieval algorithm for NASA's ICESat-2 photon-counting laser altimeter. *Remote Sensing of Environment*, 233, 111352.

Smith, B., H. A. Fricker, A. Gardner, M. R. Siegfried, S. Adusumilli, B. M. Csathó, N. Holschuh, J. Nilsson, F. S. Paolo, and the ICESat-2 Science Team, 2020. ATLAS/ICESat-2 L3A Land Ice Height, Version 3. [Indicate subset used]. Boulder, Colorado USA. NASA National Snow and Ice Data Center Distributed Active Archive Center. doi: https://doi.org/10.5067/ATLAS/ATL06.003. [Date Accessed].

Stuart, K. M., & Long, D. G., 2011. Tracking large tabular icebergs using the SeaWinds Ku-band microwave scatterometer. *Deep Sea Research Part II: Topical Studies in Oceanography*, 58(11-12), 1285-1300.

Wesche, C., & Dierking, W., 2012. Iceberg signatures and detection in SAR images in two test regions of the Weddell Sea, Antarctica. *Journal of Glaciology*, 58(208), 325-339.

Wesche, C., & Dierking, W., 2015. Near-coastal circum-Antarctic iceberg size distributions determined from Synthetic Aperture Radar images. *Remote Sensing of Environment*, 156, 561-569.

Yu, Q., Liu, S., Li, H., & Zhang, Q., 2017. Formula derivation and application of solar elevation angle. *Journal of Henan University of Engineering(Natural Science Edition)*, 29, 77-80.

Yuan, X., Qiao, G., Li, Y., Li, H., & Xu, R., 2020. Modelling of glacier and ice sheet micro-topography based on unmanned aerial vehicle data, Antarctica. *The International Archives of Photogrammetry, Remote Sensing and Spatial Information Sciences*, 43, 919-923.